IAC-20- C4.8-B4.5A.11.x58225

Flow regime characterization of a MEMS-based vaporizing liquid microthruster

Fontanarosa D.ᵃ*, Francioso L.ᵇ, De Giorgi M. G.ᵃ, De Pascali C.ᵇ, Ficarella A.ᵃ, Vetrano M. R.ᶜ

[a] *Dept. of Engineering for Innovation, University of Salento, via per Monteroni, Lecce I-73100, Italy*,
donato.fontanarosa@unisalento.it
[b] *Institute for Microelectronics and Microsystems IMM-CNR, Via per Monteroni "Campus Ecotekne", Lecce, Italy*
[c] *Dept. Of Mechanical Engineering, KU Leuven, Celestijnenlaan 300A postbus 2421, B-3001 Heverlee, Belgium*

* Corresponding Author

Abstract

The present work discusses an experimental investigation of the flow into a MEMS-based vaporizing liquid microthruster equipped with sensing capabilities and low-power on-channel secondary heaters. The sensing capabilities (Resistance Temperature Detectors and capacitive void fraction sensors) are used to investigate the flow instability and for performance control. The device has a sandwich structure, composed of a silicon substrate and a glass substrate: this last one allows optical access into the device. The main heating of the propellant is provided by means of a Platinum resistive heater placed on the bottom of the silicon layer.

Three flow regimes have been detected and investigated: fully liquid flow, two-phase flow and fully vaporized flow. Their dynamics has been captured by means of high-speed micro-flow visualizations under rough vacuum conditions (about 29 kPa). Furthermore, the expansion of the exhaust vapor plume exiting from the micronozzle has been analysed vis Schlieren visualizations. Results highlighted the cyclic behaviour of the liquid-vapor flow into the inlet chamber and the micronozzle regions during the two-phase flow regime, while at the micronozzle the flow is still two-phase. Once the fully vaporized flow regime is established, the two-phase flow dynamics into the inlet chamber becomes more stable with complete filling and a more uniform distribution of the flow between microchannels. Schlieren imaging captured the increase of the exhaust plume spreading half-angle when moving from external ambient condition towards rough vacuum.

Keywords: electric micro-propulsion; small satellites; vaporizing liquid micro-resistojet; MEMS technology; flow regime characterization

Nomenclature

$\dot{m}$, MFR	mass flow rate [kg/s]
$\dot{Q}_{vap}$	heat required for full vaporization and overheat [W]
P_{el}	electrical dissipated power [W]
T_{exit}	temperature recorded close to the microchannels exit [T]
t	time [s]
$\Delta V_{satellite}$	satellite velocity increment [m/s]
$\mathcal{V}$	propellant volume [cm³]
η_h	heating efficiency

Acronyms/Abbreviations

HTCC	High-Temperature Co-fired Ceramics
LED	Light Emission Diode
LTCC	Low-Temperature Co-fired Ceramics
MEMS	Micro-Electro-Mechanical System
MF-HSvis	Micro-Flow High-Speed visualization
RTD	Resistance Temperature Detector
VFS	Void Fraction Sensor
VLM	Vaporizing Liquid Microthruster

1. Introduction

The first development of the VLMs dates back to Mueller's studies [1,2,3], who first manufactured a silicon-based MEMS device, characterized the heat losses in relation to its packaging, and evaluated the influence of feeding pressure on the vaporization process. Later, different configurations, materials and manufacturing technologies have been investigated, as summarized in [4].

Concerning the silicon technology, Mukejee et al. [5] developed a MEMS-based micro-thruster by means of wet anisotropic etching. Water was used as propellant, and experiments showed thrust force magnitudes ranging between 0.15 mN and 0.46 mN. Similarly, Maurya et al. [6] first designed and fabricated a silicon-based VLM with an integrated micro-heater. Their micro-thruster achieved thrust forces in the range 5 μN to 120 μN, with a heating power between 1 W and 2.4 W using water as propellant. Later, Kundu et al. [7] designed a new single-channel VLM characterized by a more uniform heating ensured by two integrated heaters, which allowed to reach a thrust force of 1 mN using maximum heater power of 3.6 W. Instead, Ye et al. [8] designed a VLM

characterized by a pulsated heating by means of the application of an electric pulse. Their micro-thruster exhibited a total impulse of $0.2x10^{-6}$ Ns produced in a second with pulse power of 30 W. Instead, Chen et al. [9] investigated the two-phase flow characteristics in a single channel silicon-based VLM, observing four different flow patterns, i.e. snake flow, vapor-droplet flow, vapor-droplet-jet flow and vapor flow. More recently, Kwan et al. [10] designed a low power (8 W) water-fed vaporizing liquid microthruster operating in the Leidenfrost boiling regime.

Concerning new materials and manufacturing technologies, Karthikeyan et al. [11] first developed a low temperature co-fired ceramic (LTCC), demonstrating that the LTCC can replace the silicon, owing to good electrical conductivity of printed metallization, a relative low cost for mass production, and a relatively simple and fast fabrication process. Later, Cheah and Low [12] successfully tested a high temperature co-fired ceramic (HTCC) microthruster characterized by a three layers structure with a platinum-based microheater. Even though the proposed ceramics-based VLM exhibited an improved specific impulse efficiency and a reduction of the electrical power consumption, the silicon-based MEMS technology still ensure improved manufacturing flexibility and micro-electrical system integration capability, as confirmed by the more intensive

All the previously cited works investigated a single-channel configuration. Instead, Cen and Xu [13] first fabricated a MEMS-based VLM made by parallel microchannels and focused on the characterization the flow boiling instabilities in relation to the measured performance. In addition, they found that, if the device is not properly pre-heated before the propellant injection, the snake flow pattern can lead to the failure of the micro-thruster. More recently, Silva et al. [14] developed a new VLM with integrated molybdenum heaters and temperature sensing using water as green propellant able to meet the strict requirements of the CubeSats and PocketQubes programs. Recently, Liu et al. [15,16] developed and tested two new concepts of VLM using induction heating, characterized by tubular and planar geometry, respectively.

In all the devices discussed above, the flow behaviour into the VLM has demonstrated to be intrinsically instable. In fact, flow boiling instabilities usually occur into inlet and heating chambers causing pressure – temperature – mass flow rate oscillations, which dramatically affect the expansion process into the micronozzle, and, hence, the microthruster performance. To this concern, a MEMS-based VLM prototype has been designed and manufactured, equipped with a set of temperature and vapor quality sensors for the flow

instability control. Furthermore, secondary low-power platinum resistive heaters have been placed into the single channel volume for fine flow control by localized heating operation. The operational feasibility of the microthruster has been previously demonstrated, which allowed for the detection of three main flow regimes: fully liquefied flow, two-phase flow and fully vaporized flow regimes. Based on those findings, a deeper investigation has been performed in order to characterize the flow dynamics of each flow regime. To this purpose, micro-flow high-speed visualizations have been performed in order to investigate the dynamics of the micro boiling flow into the device. Instead, Schlieren imaging allowed to capture the appearance of the exhaust plume in presence of full vaporized flow condition and its modification when moving from external ambient condition to rough vacuum.

2. Device description

The microthruster fabrication process was performed at the clean room facilities owned by the Italian National Research Council - Institute of Microelectronics and Microsystems (CNR-IMM) in Lecce (Italy), with a custom process flow that integrates different pattern transfer techniques, vacuum depositions, deep dry etching of silicon, front-back lithography alignment steps and adhesive silicon-glass bonding. Figure 1 shows a picture of the fabricated VLM with indication of the main sub-systems and integrated sub-structures.
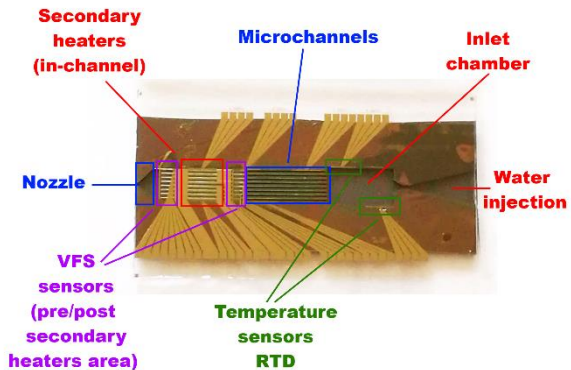

Figure 1: Schematics of the MEMS microthruster: outer dimensions are 20 x 7 mm^2.

As reported in [17], the device has a length of 20 mm, a width of 7 mm, and a total thickness of 500 μm, while the etching depth for each channel is 230 μm. The length and the thickness of the glass pad are equal to the silicon substrate; on the contrary, its width is equal to 9 mm. In this way, space is allowed for the electric connection pads of both the sensors and the secondary heaters. A V-shaped inlet of about 2 mm length ensures water feeding inside the chip using a 33G needle, fixed to the device using an epoxy resin (type Loctite 9492) that provides the proper junction tightness. Eight microchannels of 90 μm

IAC-20- C4.8-B4.5A.11.x58225

Page 2 of

width and 9 mm length compose the heating chamber. This design should maximize the heat transfer coefficient, reduce the pressure losses, and hinder the flow boiling instabilities. Microchannels are spaced apart of 130 μm. The convergent-divergent planar micronozzle, has a throat width of 150 μm, the angle of the convergence section of 45°, while the divergent section owns 30°. A high divergence angle is chosen to mitigate the viscous losses due to the boundary layer growth normal to the planar walls, as demonstrated in [18,19].

Concerning the integrated electrical sub-system, a thin film Platinum heater, placed on the bottom of the silicon substrate, provides the heat to the propellant fluid (the metallic structure highlighted in Figure 2(b)). Furthermore, a set of capacitive void fraction sensors (VFSs) and 4-wires resistance temperature detectors (RTDs) are embedded in the device, to provide sensing capabilities for the flow control inside the microthruster. Furthermore, secondary resistive heaters have been patterned, using photolithography, on the glass substrate as additional low-power heating for flow control test. It is worth observing that RTDs have been placed along the device in the proximity of the fluid region, in order to detect as much as possible by the local variation state of the fluid temperature. On the contrary, both secondary heaters and VFSs are located directly into the microchannels.

The device uses water as propellant: the trade-off between propulsive performance, safety, and any other desired features such as density, heat capacity, storability and availability, usually lead to the choice of the propellant.
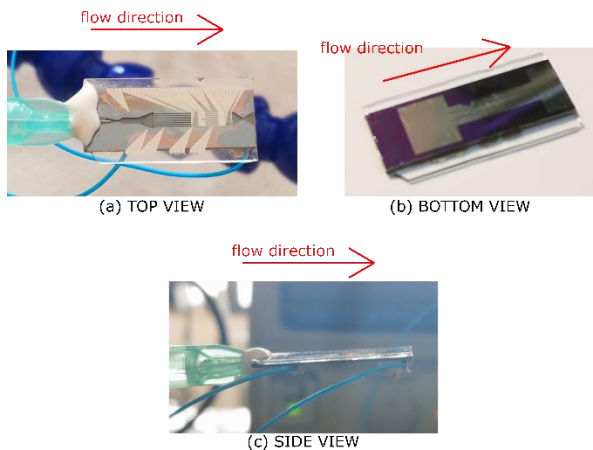

Figure 2: Picture of a VLM prototype: (a) top view; (b) bottom view; (c) side view.

In [20] the concept of green propellant was related to the capability in satisfying requirements in terms of propulsive performance (associated mainly to thrust and specific impulse), system density (associated to mass and size), and safety (associated to flammability, instability

and health hazard). Their analysis led to the choice of liquid water as the best green propellant for use in VLMs: it can ensure thrust forces from 0.1 mN to 10 mN, and specific impulse $I_{sp} > 100$ s using heating power ranging between 4 W and 12 W. This could allow increment of satellite velocity per unit volume of propellant $\Delta V_{satellite}/\mathcal{V}$ above 0.25 m/s/cm^3, in combination with ultra-safe operational environment, low pollutant impact, and high-density design. A greater power consumption due to the high enthalpy of vaporization is the most relevant drawback, even though it can be more relaxed as it also depends on other design factors, e.g. structural design, solar panel design, and mission design.

3. Experimental methodology and setup

3.1 Previous preliminary characterization of flow regimes based on embedded micro-sensors data

A custom experimental setup was previously designed to characterize the sensors and actuators embedded into the fabricated microthrusters. The experimental apparatus is shown in Figure 3: a high precision micro-probing system composed of 8 probes were used to acquire the signals of embedded micro-sensors. The device under investigation was turned upside down and housed in a Teflon sheet specifically shaped to give optical access to the camera placed behind the microthruster and in front of the glass.
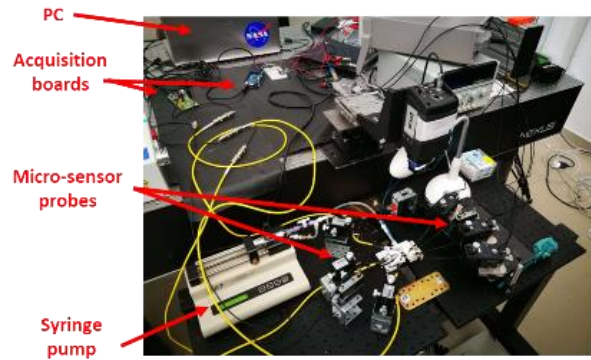

Figure 3: Experimental apparatus: micro-sensor acquisition system.

Distilled water was pumped into the microthruster device using a Cole-Parmer 74900 series single-syringe pump (accuracy ±0.5\% of reading) through the injection needle. The syringe pump controlled the water mass flow rate in the device. A commercial pressure transducer working in the range 0-100 psi (accuracy ±2\% full scale) measured the inlet feeding pressure. The bench power supply ISO-TECH IPS-2303S was used to supply the voltage to the main heater and measure the resulting electrical current.

An Arduino Mega 2560 board was used to acquire the devices (pressure and RTD signals). The module type

HiLetgo PT100 MAX31865 was used for RTD signal amplification before reading. The temperature recorded close to the microchannels exit, i.e., T_{exit}, and the electrical dissipated power P_{el} provide together a preliminary regime characterization at different mass flow rates and external ambient conditions.
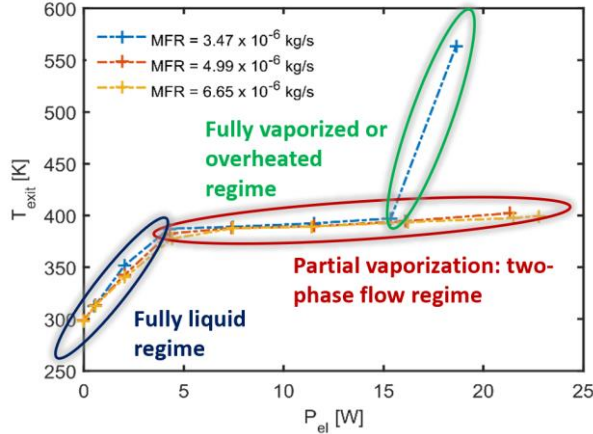

Figure 4: RTD temperature T_{exit} as a function of the electrical dissipated power P_{el}. *MFR* in the legend denotes the mass flow rate.

As summarized in Figure 4, three different flow regimes were clearly detected: the fully liquefied flow regime, the two-phase flow regime and the fully vaporized flow regime. The fully liquefied flow regime occurred before flow reached saturation conditions ($P_{el} < 5$ W and $T_{exit} < T_{sat}=373$ K). In this regime, the flow stream temperature linearly increases with the voltage applied to the heater. This regime is also characterized by constant feeding pressure, i.e., there are no significant changes of the fluid properties and the flow is driven by a similar pressure drop. At $P_{el} > 5$ W, water vaporization occurred, and the two-phase flow regime established into the microchannels. During this regime, T_{exit} was almost constant and equal to the saturation temperature: as P_{el} increased, the vapor fraction at the microchannel exit approached to the unity. When reducing the mass flow rates at 3.47×10^{-6} kg/s, the fully vaporized regime occurred at about 18 W, as confirmed by the measured strong vapor overheating ($T_{exit}=563$ K). It is worth underlying that the theoretical required power for vaporization and over-heating is about 10.3 W. Hence, the heating efficiency, $\eta_h = \dot{Q}_{vap}/P_{el}$, resulted equal to 0.553, indicating that about 44.7% of the electrical power was thermally dissipated (convection, conduction and radiation). This finding pointed out the importance of a performant thermal insulation to ensure proper energy conversion for this kind of micro-propulsion systems.

3.2 Imaging-based experimental setup for flow regime characterization

Based on the results of the experiments performed at ambient conditions, a new experimental campaign was carried out at the Department of Mechanical Engineering, KU Leuven (Belgium). This campaign was focussed on a more detailed characterization of the micro-flow behaviour into device. The investigation consisted in two parts:
- micro-flow high-speed visualizations of the boiling flow into the inlet chamber and micronozzle;
- Schlieren imaging of the exhaust plume.

3.2.1 Micro-flow high-speed visualizations
A schematic of the experimental setup developed for the high-speed visualizations is shown in Figure 5. Figure 6 includes some pictures of the overall experimental apparatus. This one consisted in a cylindrical vacuum chamber equipped with four flanges perpendicularly installed on the body of the chamber. Two flanges were used for optical access to the chamber thanks to circular quartz windows of about 100 mm diameter. These two optical accesses were positioned on the opposite sides of the chamber, along the same axis. A further flange placed on the top of the chamber was equipped with both the fluidic and the electrical feedthroughs.
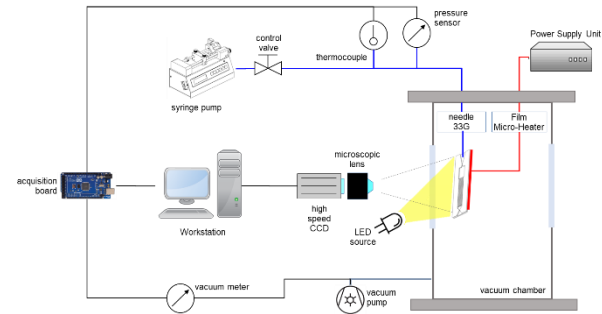

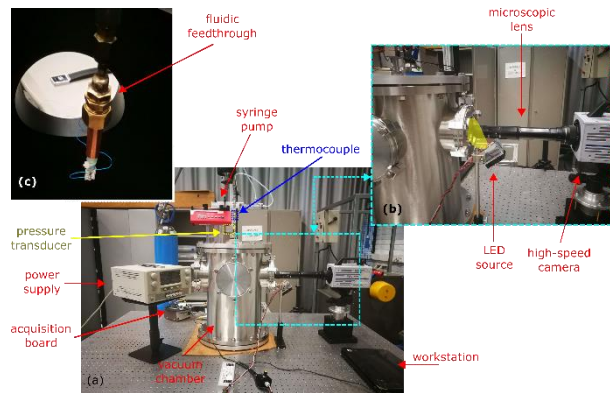Figure 5: Sketch of the micro-flow high-speed visualization setup.

Figure 6: Micro-flow high-speed visualization setup: detailed view.

A rotary vane vacuum pump (model Edwards RV3 04893) coupled with a control valve allowed to manually control the vacuum level into the chamber up to about 10 Pa. The water feeding was performed using a programmable syringe pump (model NE-1000) coupled with a 100 ml syringe. The syringe pump allowed to control the water mass flow rate injected into the microthruster. Along the feeding line, a K-type thermocouple and a Validyne DP-15 variable reluctance differential pressure transducer coupled with a carrier demodulator type Validyne CD-15 allowed for the measurement of the feeding temperature and pressure, respectively. All sensor data were acquired using an Arduino Mega 2560 board at 20 Hz.

Furthermore, a direct current power supply unit (model BST PSM 2/5A) allowed for the electrical feeding of the main heater of the microthruster, which was mounted into the vacuum chamber close to the optical windows in front of the acquisition systems. This last one was arranged outside the vacuum chamber, and it composed of a high-speed camera Photron FastCam SA/3 and a programmable LED light source (model Cree XLamp CXB3590, 137 W maximum radiant flux) for frontal illumination of the microthruster. A microscopic lens model 12X Zoom Navitar mounted on the camera allowed for high-resolution acquisition of the flow into the microthruster.

Flow images were captured with resolution of 1024 pixels x 768 pixels, exposure time of 0.001 ms and acquisition rate of 1000 Hz. At each pixel point, the image grey level was discretized on 256 grey levels (using 8 bits), defining the full dark condition (ultra-low luminosity) and the full bright condition (ultra-high luminosity).

3.2.2 Schlieren Imaging

As shown in Figure 7, the Schlieren Imaging setup consisted in a Z-type 2-mirror Schlieren systems composed by 2 parabolic mirrors with 100 mm of diameter and 1000 mm of focus length, a programmable LED light source (model Cree XLamp CXB3590, 137 W maximum radiant flux), a pinole, a knife and the Photron FastCam SA/3 high-speed camera equipped with Sigma Macro lens 105 mm with aperture set at f2.8 and two Tamron-F AF tele-converters. The LED light is first collected into a diffusing tube of 50 cm length, then a dichroic achromatic lens of 42 mm diameter, focuses it in correspondence of a pinhole diaphragm set with the minimum aperture of about 2 mm. The light beam is reflected by the first parabolic mirror, crosses the chamber, passes through the thrust plume and is reflected by the second parabolic mirror to the camera. The knife edge is placed at the focal point of the reflected plume image and precisely positioned to adjust the density gradient in the obtained Schlieren images.
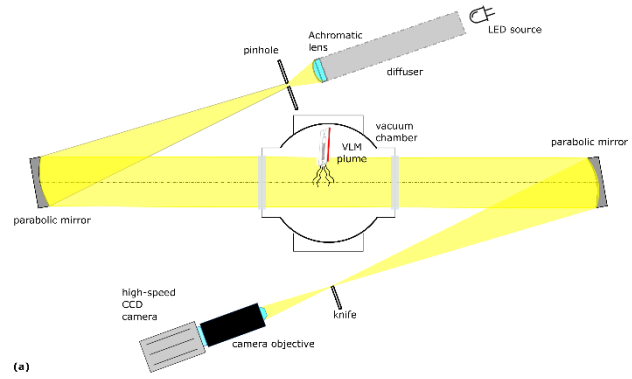

Figure 7: Sketch of the z-Schlieren setup.

The images were captured with a resolution of 1024 pixels x 1024 pixels, exposure time of 0.0005 s and acquisition rate of 2000 Hz. The image dataset was processed by using Matlab® with user-defined routines. In particular, the grayscale of each raw image (see Figure 8(a)) was normalized to obtain the relative luminance field $I(t)$, ranging between 0 and 1. The average image $\bar{I}$ was the removed from each luminance field, i.e. $I' = I(t) - \bar{I}$. The obtained fluctuating luminance I' was then amplified by re-scaling the color map between the minimum and the maximum values (see Figure 8(b)).
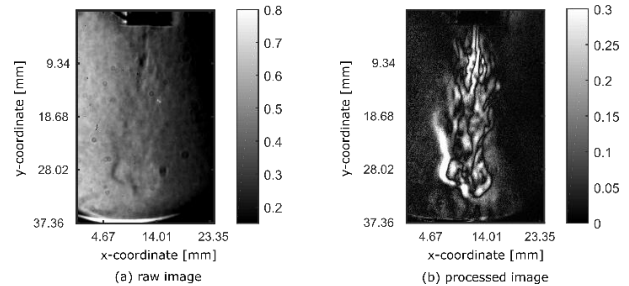

Figure 8: Processing of the Schlieren plume image: (a) raw image; (b) post-processed image.

4. Imaging-based flow regime characterization

Tests were carried out in order to perform a qualitative analysis of the flow behaviour for each flow regime observed during the preliminary tests reported in Sec. 3.1, namely fully liquified flow regime, two-phase flow regime and fully vaporized flow regime. Table 1 presents the experimental test matrix of the high-speed visualizations of the boiling flow into the microthruster. In particular these tests were carried out by varying the electrical power at constant mass flow rate $\dot{m} = 4.17x10^{-6}$ kg/s and average vacuum level of about $p_a = 29.12$ kPa (test cases 1 to 5). The experimental campaign started at ambient pressure conditions into the vacuum chamber, and pre-heating the microthruster by applying 1.26 W of electrical power (corresponding to applied voltage of 1.4 V) for 5 minutes in empty dry configuration ($\dot{m} = 0$ kg/s). Once the injection started, a

fully liquified flow regime was established into the microthruster, and the feeding pressure p_0 increased up to about 142 kPa due to the hydraulic resistance of all the system. Once p_0 was stable, the vacuum pump was activated and the vacuum level into the chamber was gradually reduced. The feeding pressure also reduced, due to the pressure drop into the vacuum chamber and the presence of the liquid flow into the microthruster.

The vacuum level was fixed at $p_a = 29.12$ kPa, corresponding to a pressure slightly higher than the minimum feeding pressure detectable by the pressure transducer of about 100 kPa. High-speed acquisition started once steady state conditions were reached upstream the injection and into the vacuum chamber. During the experiment, the voltage applied to the main heater, was gradually increased in several steps. Visualizations of the flow into the inlet chamber and into the micronozzle, were separately performed after 3 minutes from the establishment of the desired flow regime. Results are shown in Figures 9, 10, 11, 12 and 13, corresponding to the fully liquified flow regime immediately after pre-heating at $P_{el}=1.3$ W (test case 1), the fully liquified flow regime at $P_{el}=3.1$ W (test case 2), the two-phase flow regimes at $P_{el} = 6.2$ W (test case 3) and $P_{el} = 9.6$ W (test case 4), and the fully vaporized regime at $P_{el} = 13$ W (test case 5).

Table 1: Experimental test matrix. Mass flow rate $\dot{m} = 4.17x10^{-6}$ kg/s. Feeding pressure: $p_0 = 100$ kPa under vacuumed conditions; $p_0 = 142$ kPa at ambient conditions.

Test case	P_{el} [W]	p_a [kPa]	Flow regime	Optical technique
1	1.3	29.12	fully liquified	MF-HSvis*
2	3.1	29.12	fully liquified	MF-HSvis*
3	6.2	29.12	two-phase	MF-HSvis*
4	9.6	29.12	two-phase	MF-HSvis*
5	13	29.12	Fully vaporized	MF-HSvis*
6	15.7	101.35	Fully vaporized	SCHLIEREN
7	12.4	29.12	Fully vaporized	SCHLIEREN

*MF-HSvis: Micro-Flow High-Speed visualization

When just pre-heated at low electrical power, the flow into the microthruster remained liquid both into the inlet chamber and in the micronozzle. At the micronozzle exit, one single droplet was formed before being detached due to gravity and followed by a new droplet growth and detachment (see Fig. 9(b)).
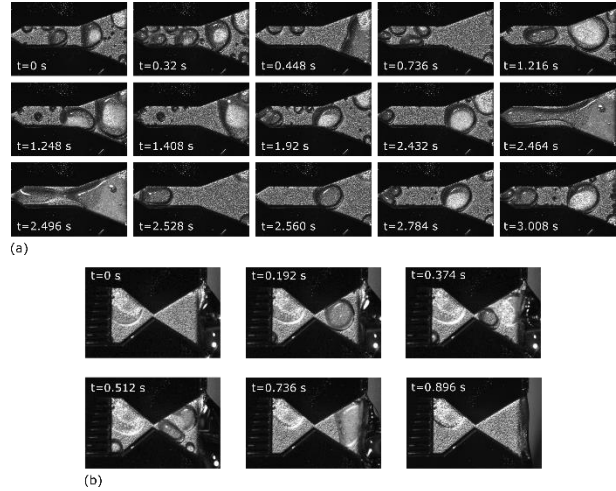

Figure 9: Temporal sequence of the fully liquified flow regime immediately after pre-heating at $P_{el} = 1.3$ W (test case 1): flow visualization into the inlet chamber (a) and the micronozzle (b).

This cyclic behaviour affected the pressure drop upstream, as highlighted by the multiple droplets crossing the micronozzle and caused by the chocking at the micronozzle throat. Consequently, the liquid feeding through the inlet chamber was discontinuous, as highlighted in Fig. 9(a). Here, small droplets were released by the feeding needle, crossed the constant section coalescing each other and forming a large droplet into the divergent region. This large droplet anchored to the microchannels entrance. Water was then fed into the microchannels up to the complete ejection of the large droplet. During the large droplet ejection, new droplets were injected by the needle and a new coalescence process started. Sometimes, the flow exhibited a rapid ejection and the full filling of the inlet chamber, e.g. at $t = 2.464$ s and $t = 2.496$ s, probably due to a short temporal improvement of the heat transfer coefficient.
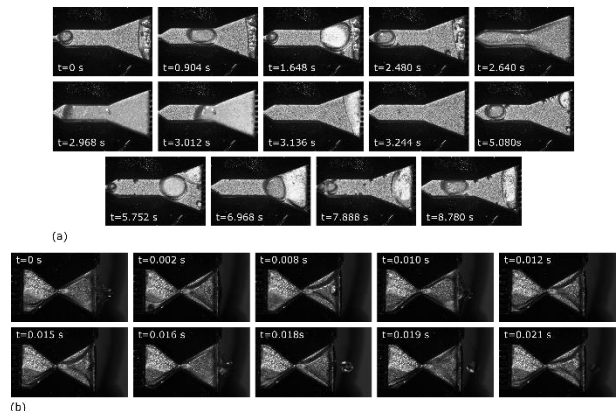

Figure 10: Temporal sequence of the fully liquified flow regime $P_{el} = 3.1$ W (test case 2): flow visualization into the inlet chamber (a) and the micronozzle (b).

When the electrical power increased at P_{el} = 3.1 W (test case 2), heating effects starts to have an impact on the flow behaviour. As shown in Figure 10(a), the droplet cycle became more regular and slower with respect to the test case 1. One single droplet was continuously injected by the feeding needle, crossed the constant section region and elongated due to thermal expansion. Then, it grew and partially vaporized into the divergent region, as highlighted by the white level increase at t = 1.648 s, before anchoring at the microchannels entrance and being ejected through them. Again, sometimes the flow experienced the rapid ejection through the inlet chamber with a complete filling, e.g. at t = 0.264 s. The flow into the micronozzle also became more regular (see Fig. 10(b)) since the convergent region was always well filled with liquid water, as well as the divergent region. Into the divergent region, the heat flux at walls was coupled with the formation of the vena contracta downstream to the micronozzle throat, inducing high-frequency oscillations of the liquid-vapor interface. Consequently, the flow exhibited a continuous modification of the fluidic geometry of the micronozzle, with a shrinking-enlarging cyclic dynamic which led to the axial ejection a single droplet at the micronozzle exit, e.g. at t = 0.018 s.
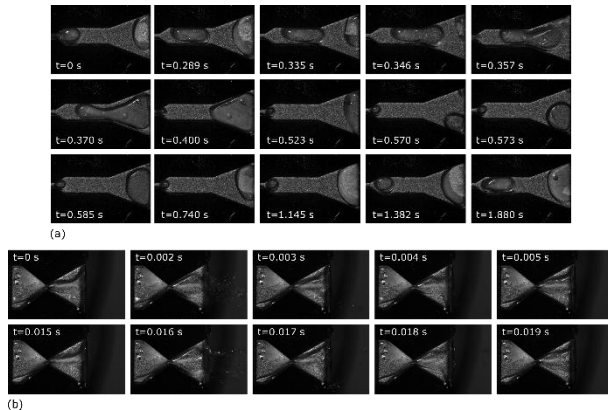

Figure 11: Temporal sequence of the two-phase flow regime at P_{el} = 6.2 W (test case 3): flow visualization into the inlet chamber (a) and the micronozzle (b).

When the electrical power was further increased at P_{el} = 6.2 W (test case 3), the flow was still mainly liquid into the inlet chamber, but flow boiling instabilities were experienced and a liquid-vapor exhaust plume was observed at the micronozzle exit. Figure11(a) shows that one single droplet was injected by the feeding needle, and it rapidly grew when moving towards the microchannels entrance region. During its ejection through the microchannels, reverse flow boiling instabilities occurred inside them. This can be observed in the frames going from t = 0.570 s to t = 0.585 s by the enlargement of the droplet placed on the bottom of the divergent region and anchored to the microchannels inlet.

Into the micronozzle, the flow exhibited the same high-frequency dynamics of the vena contracta observed in the previous flow regime (test case 2), even though with a more unstable behaviour due to the stronger vaporization process. This resulted in the ejection of a finer spray symmetrically expelled at the micronozzle exit, as highlighted in Figure11(b) at t = 0.002 s and t = 0.016 s, with similar periodicity with respect to the previous flow regime (test case 2).
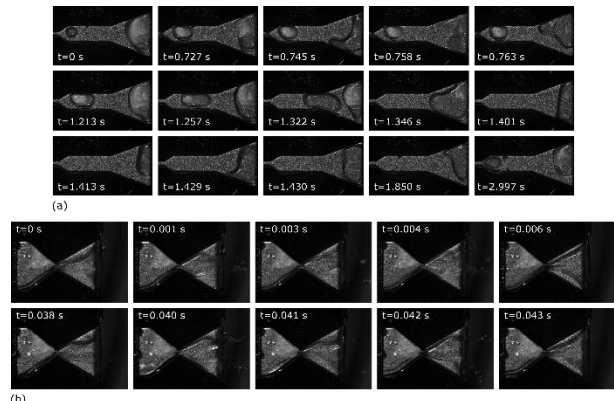

Figure 12: Temporal sequence of the two-phase flow regime at P_{el} = 9.6 W (test case 4): flow visualization into the inlet chamber (a) and the micronozzle (b).

When increasing the electrical power at P_{el} = 9.6 W, the two-phase flow regime was still established into the microthruster, with no relevant modifications of the main flow characteristics. However, Figure12(a) shows that the reverse flow boiling instabilities, occurring into the microchannels, became more evident, e.g. at t=0.745 s and t = 1.429 s, as well as the explosive boiling phenomenon rarely occurred into the divergent region (t = 0.763 s). Instead, a finer spray (see Fig. 12(b)) and a more vaporized exhaust plume was observed at the micronozzle exit.
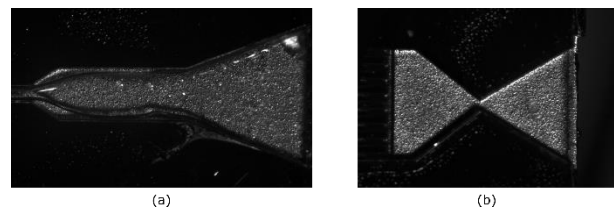

Figure 13: Fully vaporized flow regime at P_{el} = 13 W (test case 5): flow visualization into the inlet chamber (a) and the micronozzle (b).

The fully vaporized flow regime was observed at P_{el} = 13 W (test case 5). It represents the design operating condition in terms of propulsive performance. In fact, during this regime there was a stable full filling of the inlet chamber, and no reverse flow from microchannels was retrieved (see Figure13(a)). Also, the flow was

completely vaporized into the micronozzle, as shown in Figure13(b).

The fully vaporized flow regime operated for about 25 minutes. It is worth to underline that, a strong relation between the electrical properties of the main heater, related to the temperature of the device, and the heat flux exchanged between the device and the propellant, was observed. In particular, the temperature of the thruster increased due to the reduction of the heat transfer coefficient once the full vaporized flow conditions established. While heating, the main heater resistance also increased with temperature. Thus, the electrical current reduced from 2.82 A up to 2.35 A, and the electrical power reduced too. Therefore, the heat provided to the device started to reduce, as well as its temperature and the main heater resistance too. Hence, the current began to increase up to 2.80 A, and the power also increased enhancing the heating. Therefore, a new electro-thermal cycle started, as highlighted in Figure 14: when the electrical power rose up to accomplish the complete vaporization of the flow, the heating and the temperature rose too, leading to the increase of the heater resistance; consequently, the electrical current went down. Therefore, electrical power reduced and the device started to cool down in combination with the appearance of the spray at the micronozzle exit: this brought to the reduction of the main heater resistance and the following rise of the electrical current: hence, the electrical power increased again up and the fully vaporized flow regime was recovered.
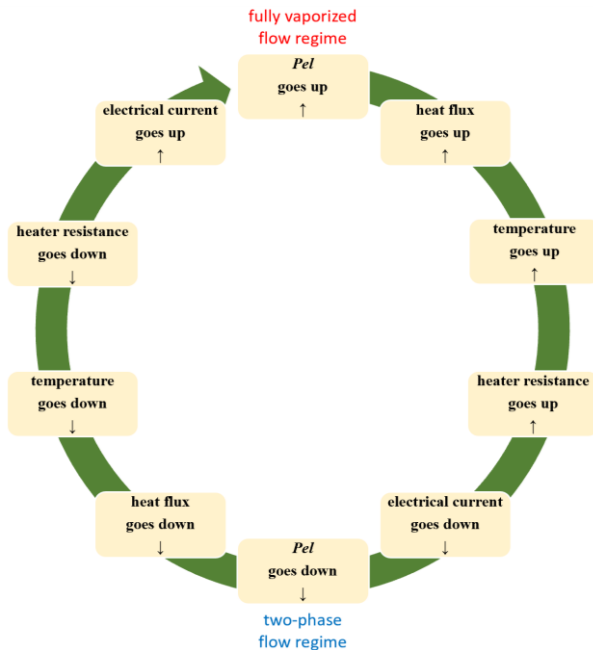

Figure 14: Electro-thermal cycle established at the inception conditions of the fully vaporized flow regime.

This intrinsic unstable behaviour suggested that the heating process must be controlled for flow stabilization by temperature, instead of by electrical power. To this purpose, this VLM must be equipped with micro-controller in combination with the designed embedded micro-sensing and secondary heating capabilities.

Schlieren imaging allowed for the characterization of the exhaust plume in fully vaporized flow regime, at ambient pressure (test case 6) and the same vacuum conditions used for micro-flow visualizations (test case 7).
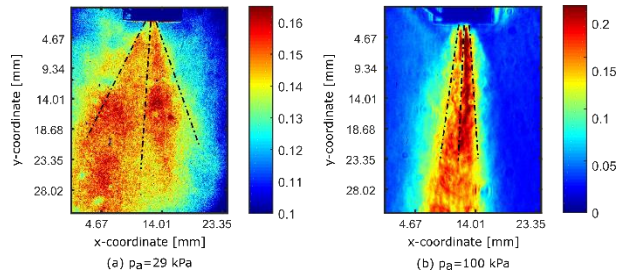

Figure 15: Average plume appearance resulting from Schlieren imaging: (a) p_a = 29.1 kPa, test case 7 (jet spreading half-angle equal to 20°); (b) p_a= 101.35 kPa, test case 6 (jet spreading half-angle equal to 5°).

Figure 15 shows the comparison of the average plume shape. In particular, when operating at ambient pressure, the flow was subsonic at the micronozzle exit, highly turbulent and hot. This was confirmed into the Schlieren image in Figure15(b), which shows a higher intensity of the plume due to stronger density gradients through it. Instead, when operating under rough vacuum conditions, the flow exhibits a better expansion, as confirmed by the exhaust plume spreading half-angle which increased from 5° at ambient pressure to 20° at a=29.12 kPa (see Figure 15(a)). Moreover, under vacuumed condition, the Schlieren image intensity of the vapor plume was weaker than the one observed at ambient pressure, since the increased gas rarefaction condition and a lower gas temperature reduced the density gradient through the jet. It is worth highlighting that no shock wave phenomena have been observed, probably due to the absence of the proper discharge pressure required for the adapted nozzle condition, as well as the viscous effects into the micronozzle caused by the boundary layer growth.

5. Concluding remarks and future steps

The present work discusses an experimental investigation of the flow into a MEMS vaporizing liquid microthruster (VLM) for micro and nano-satellites attitude control. The device has a sandwich structure, composed of: i) silicon substate onto which the VLM geometries have been fabricated using anisotropic wet

etching; ii) glass substrate which allows for the optical access. The two substrates are glued to each other by means of thermo-compressive bonding. The heating of the propellant is provided by means of a Platinum resistive heater placed on the bottom of the silicon die. In addition, the device has been equipped with a set of temperature and void fraction micro-sensors, and low-power on-channel secondary heaters in order to enable sensing capabilities for the flow instability and performance control.

Water was used as propellant. Three flow regimes have been detected and investigated: fully liquid flow, two-phase flow and fully vaporized flow. Their dynamics has been captured by means of high-speed micro-flow visualizations under rough vacuum conditions (about 29 kPa). Furthermore, the expansion of the exhaust vapor plume exiting from the micronozzle has been analysed. Results highlighted the cyclic behaviour of the liquid-vapor flow into the inlet chamber and the micronozzle regions during the two-phase flow regime. Discrete droplets are released from the injection needle; hence, they coalesce inside the inlet chamber forming a single large flow structure. Its collapse occurs when the water enters the microchannels where the vaporization process is speeded up. At the micronozzle the flow is still two-phase: the convergent part is well filled, while a vena contracta with two clear vapor pockets forms on the solid inner walls. Furthermore, the boiling flow promotes the establishment of a spray with decreasing droplet size as the heating is increased and the fully vaporized flow is reached. When established, the fully vaporized flow exhibited a more stable two-phase flow dynamics into the inlet chamber with full filling and a more uniform distribution of the flow between microchannels, while the micronozzle is dry. Schlieren imaging allowed to quantify the improvement of the flow expansion when moving from external ambient condition to rough vacuum: the exhaust plume spreading half-angle which increased from 5° at ambient pressure to 20°.

Furthermore, the present work figured out the intrinsic instability of such kind of microthruster, related to the two-phase flow nature of its functioning. In particular, an electro-thermal cycle establishes due to the coupling between temperature, heat flux, the flow regime and its vapor content, and the main heater resistance. In addition, the rapid modification of the heat transfer coefficient, occurring when fully vaporized flow regime is established, can easily lead to the device failure. Therefore, the next step will be the integration of the micro-sensors and the activation of the secondary heaters for the development of an advanced active flow control algorithm for safe thermal management and boiling flow instability hindering. To this last aspect, an optimization study of the heating system will be performed, involving the microthruster geometries, the surface micro-texturing, and the micro-heaters design.

References

[1] J. Mueller, W. Tang, A. Wallace, R. Lawton, W. Li, D. Bame, I. Chakraborty, Design, analysis and fabrication of a vaporizing liquid microthruster, in: 33rd Joint Propulsion Conference and Exhibit, 1997, p.3054.

[2] J. Mueller, D. Bame, I. Chakraborty, A. Wallace, W. Tang, R. Lawton, Proof-of-concept demonstration of a vaporizing liquid micro-thruster, in: 34th AIAA/ASME/SAE/ASEE Joint Propulsion Conference and Exhibit, 1998, p.3924.

[3] J. Mueller, I. Chakraborty, D. Bame, W. Tang, Vaporizing liquid microthruster concept: preliminary results of initial feasibility studies, in: Micropropulsion for Small Spacecraft, Reston, VA, American Institute of Aeronautics and Astronautics, Inc., Prog. Astronaut. Aeronaut. 187 (2000) 215–230.

[4] Y. Gao, Y.F. Ma, J.T. Liu, A review of the vaporizing liquid microthruster technology, in: 2014 ISFMFE – 6th International Symposium on Fluid Machinery and Fluid Engineering, 2014, pp.1–3.

[5] E. Mukerjee, A. Wallace, K. Yan, D. Howard, R. Smith, S. Collins, Vaporizing liquid microthruster, Sens. Actuators A, Phys. 83(1) (2000) 231–236, https://doi.org /10 .1016 /S0924 -4247(99)00389-1.

[6] D. Maurya, S. Das, S. Lahiri, Silicon MEMS vaporizing liquid microthruster with internal microheater, J. Micromech. Microeng. 15(5) (2005) 966.

[7] P. Kundu, T.K. Bhattacharyya, S. Das, Design, fabrication and performance evaluation of a vaporizing liquid microthruster, J. Micromech. Microeng. 22(2) (2012) 025016.

[8] X. Ye, F. Tang, H. Ding, Z. Zhou, Study of a vaporizing water microthruster, Sens. Actuators A, Phys. 89(1–2) (2001) 159–165.

[9] C.-C. Chen, C.-W. Liu, H.-C. Kan, L.-H. Hu, G.-S. Chang, M.-C. Cheng, B.-T. Dai, Simulation and experiment research on vaporizing liquid micro-thruster, Sens. Actuators A, Phys. 157(1) (2010) 140–149.

[10] Kwan, Pok-Wang, Xun Huang, and Xin Zhang. "Design and testing of a microelectromechanical-

system-based high heat flux vaporizing liquid microthruster." Acta Astronautica (2020).

[11] K. Karthikeyan, S. Chou, L. Khoong, Y. Tan, C. Lu, W. Yang, Low temperature co-fired ceramic vaporizing liquid microthruster for microspacecraft applications, Appl. Energy 97 (2012) 577–583.

[12] K. Cheah, K.-S. Low, Fabrication and performance evaluation of a high temperature co-fired ceramic vaporizing liquid microthruster, J. Micromech. Microeng. 25(1) (2015) 015013.

[13] J. Cen, J. Xu, Performance evaluation and flow visualization of a MEMS based vaporizing liquid micro-thruster, Acta Astronaut. 67(3–4) (2010) 468–482, DOI: 10.1016/j.actaastro.2010.04.009.

[14] M. Silva, D. Guerrieri, H. van Zeijl, A. Cervone, E. Gill, Vaporizing liquid microthrusters with integrated heaters and temperature measurement, Sens. Actuators A, Phys. 265 (2017) 261–274.

[15] Liu, Bendong, et al. "A new vaporizing liquid microthruster with planar induction heating." Sensors and Actuators A: Physical (2020): 112010.

[16] Liu, B., Yang, X., Wang, Y., Li, D., Gao, G., Yang, J., & Zhou, R. (2020). A tubular vaporizing liquid micro-thruster with induction heating. Heat and Mass Transfer, 1-9.

[17] De Giorgi, M. G., Francioso, L., De Pascali, C., Ficarella, A., & Fontanarosa D. (2019). Preliminary results concerning the development of a water propellant vaporizing liquid microthruster for small satellites, in 9th European Conference for Aeronautics and Space Sciences (EUCASS), Madrid, Spain, 1-4 July 2019.

[18] M.G. De Giorgi, D. Fontanarosa, A. Ficarella, Modeling viscous effects on boundary layer of rarefied gas flows inside micronozzles in the slip regime condition, Energy Proc. 148 (2018) 838–845.

[19] M.G. De Giorgi, D. Fontanarosa, A novel quasi-one-dimensional model for performance estimation of a Vaporizing Liquid Microthruster, Aerospace Science and Technology, Volume 84, 2019, Pages 1020-1034, ISSN 1270-9638, https://doi.org/10.1016/j.ast.2018.11.039.

[20] Guerrieri, D. C., Silva, M. A., Cervone, A., & Gill, E. (2017). Selection and characterization of green propellants for micro-resistojets. Journal of Heat Transfer, 139(10), 102001.

IAC-20- C4.8-B4.5A.11.x58225